Interactions in hydrogen of relativistic neon to nickel projectiles: Total charge-changing cross sections

C.-X. Chen,[1] S. Albergo,[4] Z. Caccia,[4] S. Costa,[4] H. J. Crawford,[2] M. Cronqvist,[7] J. Engelage,[2] P. Ferrando,[3] R. Fonte,[4] L. Greiner,[2] T. G. Guzik,[1] A. Insolia,[4] F. C. Jones,[5] C. N. Knott,[6] P. J. Lindstrom,[7] J. W. Mitchell,[5] R. Potenza,[4] J. Romanski,[7,4] G. V. Russo,[4] A. Soutoul,[3] O. Testard,[3] C. E. Tull,[1] C. Tuvé,[4] C. J. Waddington,[6] W. R. Webber,[8] J. P. Wefel,[1] and X. Zhang[1]

(The Transport Collaboration)

[1]*Department of Physics and Astronomy, Louisiana State University, Baton Rouge, Louisiana 70803*
[2]*Space Science Laboratory, University of California, Berkeley, California 94720*
[3]*Service d'Astrophysique, Centre d'Études de Saclay, 91191 Gif-sur-Yvette, Cedex, France*
[4]*Dipartimento di Fisica, Universita' di Catania and Istituto Nazionale di Fisica Nucleare, Sezione di Catania, Corso Italia 57, I 95129-Catania, Italy*
[5]*NASA/Goddard Space Flight Center, Greenbelt, Maryland 20771*
[6]*School of Physics and Astronomy, University of Minnesota, Minneapolis, Minnesota 55455*
[7]*Lawrence Berkeley Laboratory, 1 Cyclotron Road, Berkeley, California 94720*
[8]*Department of Astronomy, New Mexico State University, Las Cruces, New Mexico 88003*

(Received 19 November 1993)

A liquid hydrogen target was used to study the nuclear fragmentation of beams of relativistic heavy ions, ^{22}Ne to ^{58}Ni, over an energy range 400 to 900 MeV/nucleon. The experiments were carried out at the Lawrence Berkeley Laboratory Bevalac HISS facility, using the charge-velocity-rigidity method to identify the charged fragments. Here we describe the general concept of the experiment and present total charge-changing cross sections obtained from 17 separate runs. These new measured cross sections display an energy dependence which follows semiempirical model predictions. The mass dependence of the cross sections behaves as predicted by optical models, but within the experimental energy range, the optical model parameters display a clear energy dependence. The isospin of the projectile nuclei also appears to be an important factor in the interaction process.

PACS number(s): 25.75.+r, 24.10.Ht

I. INTRODUCTION

One of the keys to addressing the question of the origin of galactic cosmic rays (GCR) is to determine the composition of the matter at the sources of these particles. This composition, both elemental and isotopic, reflects the nucleosynthesis and/or selection processes that influence the composition of the cosmic rays. The GCR source composition is significantly altered by the effects of fragmentation associated with cosmic-ray transport through the interstellar medium. Hence, understanding this propagation process is necessary before these effects can be unfolded from the observed abundances and conclusions drawn about the GCR source composition. Cosmic-ray transport is partially an applied nuclear physics problem which involves a knowledge of the detailed nuclear cross sections as a function of energy for all of the species of interest. Measuring all the needed cross sections is a monumental task which may never be completed. At the very least, the key reaction cross sections must be measured and used to develop techniques to accurately predict the unmeasured cross sections. Several predictive formulas for proton-nucleus (p-A) and nucleus-nucleus (A-A) interactions have been developed by various authors [1–6], but, the discrepancies between these predictions and measurements can range from $\sim 50\%$ at lighter nuclei to more than a factor of 3 for ultraheavy nuclei. Yet, for many cosmic-ray questions, accuracies of $\leq 10\%$ are required to match the precision with which the abundances are measured.

Many of the cross sections used to develop the predictive formulas were obtained by irradiating various targets with high-energy proton beams and then studying the targets for the production of specific isotopes by using radioactive decay counting [2,7,8]. Consequently, cross sections for the production of radioactive fragments such as ^{7}Be, ^{10}Be, ^{22}Na, ^{26}Al, and unstable isotopes of Sc to Ni account for much of the early data. Only recently have production cross sections from energetic beams of heavy ions been added to the overall cross-section database [9–12]. These measurements are significant for several reasons. First, one can choose the specific projectile isotopes that are particularly relevant to some aspects of cosmic-ray propagation. Second, the fragments produced are observed directly and include the stable as well as the unstable isotopes. Third, the heavy-ion fragmentation process closely mimics what happens in interstellar space. But even with these heavy-ion beam measurements, there remain significant areas, both in projectile species and energy, where few cross sections are avail-

able, and further cross-section measurements are needed to address specific problems [8].

Part of the effort related to cross-section predictions have been devoted to a study of the concept of limiting fragmentation, which predicts that above a certain energy the cross sections become independent of energy. For light projectiles such as ^{16}O or ^{12}C, it has been suggested that limiting fragmentation begins at various energies, from several GeV/nucleon to as low as 100 MeV/nucleon [13]. The onset energy of limiting fragmentation is important since it determines the "dividing line" between fragmentation modes characterized by collective effects [14] and fragmentation dominated by single-nucleon interactions [15]. However, the results from a number of experiments have shown that determining the onset energy is not as simple as might be expected [16–20]. For example, the widely used Bradt-Peters optical model for the total inelastic cross section [21] [see Eq. (11)], which relates the cross section to the projectile and target masses, has no energy dependence, but when it is combined with a soft nucleus model [22], and energy-dependent (p-p) and (p-n) cross sections, it can be used to predict the total inelastic cross section as a function of energy [2]. Therefore, the study of total cross sections has its own significance within the overall picture of nuclear interaction systematics (see Sec. III C).

The Transport Collaboration, consisting of researchers from eight institutions in France, Italy and the USA, was established to make new measurements of heavy-ion fragmentation relevant to cosmic-ray physics [23]. This collaboration has three major goals: (1) to provide measurements of critical fragmentation cross sections and to study the cross section systematics, (2) to improve the theoretical development of galactic cosmic-ray propagation, and (3) to apply the theoretical and experimental effort to improving the interpretation of cosmic-ray data. We have successfully conducted two major experimental runs, one in April, 1990, and another in April, 1991, using the Lawrence Berkeley Laboratory HISS facility [24] to collect data on 19 projectiles ranging in mass from ^{4}He to ^{58}Ni and in energy from 400 to 900 MeV/nucleon. These projectiles interacted in a liquid-hydrogen target. Table I lists species and projectile energies, both as delivered by the accelerator ("accelerator energy") and at the center of the liquid-hydrogen target ("energy at target"). Throughout this paper we will refer to a "beam" by its "accelerator energy" and projectile species (e.g., 400 MeV/nucleon ^{32}S), while results are plotted with respect to the "energy at target." Once the analysis of the beams listed in Table I is completed we would expect that over 600 new partial cross section values will be available to be incorporated into studies of nuclear interaction systematics.

Due to the sheer volume of the raw data and to the complexity of heavy-ion fragmentation information that can be revealed by the current data set, we will report the results of this program in a series of publications. This paper, the first in the series, concentrates on the general concept of the experiment, including portions of the detector setup, and reports the results of total charge-changing interaction cross sections for all of the beams except ^{4}He. These results are compared with previous measurements, as well as with various total cross-section prediction formulas, and interpreted in terms of the mass and energy dependencies.

TABLE I. Projectile species and energies.

Beam	Accelerator energy (MeV/nucleon)	Energy at target (MeV/nucleon)
^{4}He	400	392.5±0.5
^{4}He	800	794.5±0.3
^{22}Ne	400	377±2
^{22}Ne	600	581±1
^{22}Ne	910	894±1
^{26}Mg	400	371±2
^{26}Mg	600	576±2
^{32}S	400	365±2
^{32}S	600	571±2
^{32}S	800	770±2
^{36}Ar	400	361±3
^{36}Ar	600	546±2
^{36}Ar	800	765±2
^{40}Ar	393	352±3
^{40}Ca	400	357±3
^{40}Ca	600	565±3
^{40}Ca	800	763±2
^{52}Cr	400	343±4
^{58}Ni	400	338±5

II. EXPERIMENTAL TECHNIQUE

The experimental apparatus is designed to identify fragment isotopic mass (A) using the charge-velocity-rigidity technique and the formula

$$A = \frac{RZ}{\beta\gamma m_N c^2}, \tag{1}$$

where R is the fragment rigidity, Z is the charge of the projectile, β is the reduced velocity, γ is the Lorentz factor, and m_N is the nucleon mass. The entire experimental configuration is designed to provide mass and charge identification and a more detailed description of the instruments and detectors used in the experiment to determine R, Z, and β can be found elsewhere [25,26]. Below we give a brief account of the overall setup and describe the subsystem involved in obtaining the total charge-changing cross sections.

There are six primary subsystems included in the experiment: beam detection system (BDS), liquid-hydrogen target (TGT), HISS (heavy-ion spectrometer system) magnet, drift chamber (DC), time-of-flight (TOF) wall, and neutron detector (MUFFINS). Figure 1 shows the full experimental setup at the LBL HISS facility for the April, 1991 run which is essentially identical to that used during April, 1990. The accelerated beam enters the apparatus on the figure from the left and passes through the beam detection system, used to monitor incoming beam particles and to provide the experimental trigger, and the liquid-hydrogen target, in which the in-

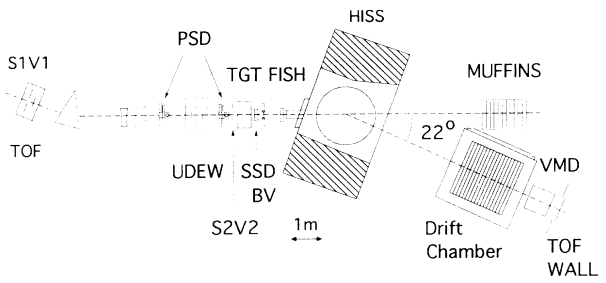

FIG. 1. Experimental setup at the LBL Bevalac HISS facility for April, 1991 run.

teraction between the projectile and proton takes place. Within the beam detection system the upstream incoming beam vector is determined by two position-sensing detectors (PSD) and the fragment charge is measured immediately after the interaction by two post target charge-sensing detectors (SSD and BV). The HISS superconducting dipole magnet separates the nuclear fragments and, combined with the upstream beam vector along with the downstream drift chamber fragment trajectory, provides the particle rigidity measurement. Particle velocity is derived from the time of flight over a total path length of $\sim$ 12 m between the upstream start trigger scintillators (S1 and S2) and the TOF wall. The TOF wall also provides another measure of the fragment charge. Finally, the neutron detector, MUFFINS [27], is aligned with the upstream beam path to study undeflected neutrons and provides information on the nuclear interaction process.

The apparatus upstream of the HISS magnet, as detailed in Fig. 2, defines the incoming beam, and determines the fragment charge. These are the essential measurements needed for obtaining the total charge-changing cross sections. The BDS consisted of two PSD's, two small plastic scintillation counters (S1 and S2), three large plastic veto scintillation paddles having holes at their centers (V1,V2,V4), a lithium-drifted silicon solid-state detector (SSD), a third small scintillation paddle (BV) and a fiber scintillator hodoscope (FISH). An individually adjustable four-scintillator anticoincidence device, UDEW (up-down-east-west), was used to select only the center portion of the beam. The readout consisted of ADC's on all detectors, TDC's on S1, S2, BV, and FISH as well as single and coincident scalers. For the April, 1990 configuration, the setup was identical with the exception that V4 was not installed. These detectors were used to establish the trigger, determining whether the event consisted of a single monoenergetic beam particle within a well-defined space geometry and time window. During the data analysis, the monitoring ADC's and TDC's were statistically analyzed to yield averages and their variances. These statistical parameters, along with proper scalar ranges, were used to set up a beam definition cut (BDC). Accepted events were within the scalar range and deviated from the average ADC, TDC values by less than ± 2.75 times the standard deviations. The purpose of this cut is to remove events that have extreme deviations from the main physical phase space, therefore eliminating unwanted possible beam contamination, various common-mode noise, and detector and electronics irregularities. Since the BDC only involves detectors that were located in front of the target, it is a nonbiased (independent of fragment species) cut.

A key component in the experiment is the cryogenic liquid-hydrogen target specially designed and constructed for this experiment by the Saclay group. While such a target can be difficult to operate and calibrate, it allows the experiment to avoid the CH_2-C subtraction method for obtaining hydrogen target cross sections that has customarily been used. The liquid-hydrogen target (TGT) provides a *direct* measurement of hydrogen interactions and reduces the amount of beam time required to obtain the same statistical uncertainty. All but the ^{4}He beam data were collected with a thin target vessel that had a depth of 0.23–0.25 g/cm^2 of liquid hydrogen to reduce multiple interactions and scattering in the target and to allow the "thin target approximation" to be used in the data analysis. The total interaction rate is $\sim$ 5% between beam projectiles and hydrogen, therefore the total secondary interaction rate is $\sim 0.05^2/2 \approx 0.1\%$, including the effective target thickness reduction. The most important parameter associated with the target is the actual thickness (in g/cm^2) of liquid hydrogen traversed by the beam particles and these values along with the liquid-hydrogen density for each individual projectile species and energy are listed in Table II. In addition to the liquid-hydrogen target, there was an exact mass equivalent dummy target which was used to determine the target out yield for the background subtraction.

The charge of fragments produced in the target are measured by the SSD and BV detectors just after the fragment leaves the target and before it has a chance to interact in any of the downstream detectors or air gaps.

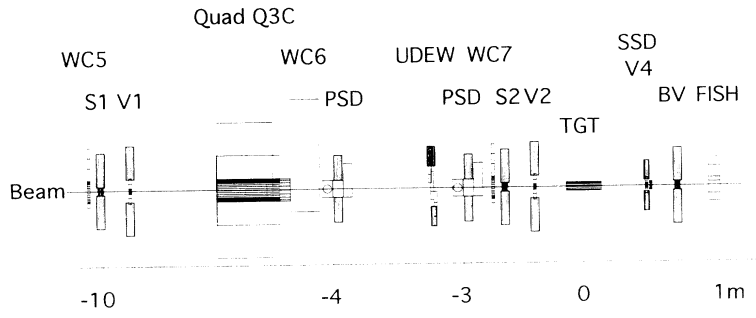

FIG. 2. Diagram of the beam detection and the target subsystems.

TABLE II. LH2 density and target thickness for all beams.

Beam	Energy (MeV/nucleon)	ρ (kg/m^3)	L (g/cm^2)
^{4}He	392.5±0.5	70.08±0.25	0.8809±0.0059
^{4}He	794.5±0.3	70.91±0.25	0.8885±0.0058
^{22}Ne	377±2	70.18±0.25	0.2401±0.0040
^{22}Ne	581±1	70.32±0.25	0.2415±0.0040
^{22}Ne	894±1	70.25±0.25	0.2388±0.0044
^{26}Mg	371±2	70.23±0.25	0.2285±0.0071
^{26}Mg	576±2	70.18±0.25	0.2359±0.0053
^{32}S	365±2	72.40±0.25	0.2553±0.0035
^{32}S	571±2	72.50±0.36	0.2511±0.0054
^{32}S	770±2	70.15±0.25	0.2406±0.0042
^{36}Ar	361±3	70.63±2.30	0.2469±0.0088
^{36}Ar	546±2	70.04±0.25	0.2388±0.0049
^{36}Ar	765±2	70.18±0.25	0.2284±0.0068
^{40}Ar	352±3	69.87±0.25	0.2346±0.0057
^{40}Ca	357±3	72.15±0.25	0.2531±0.0038
^{40}Ca	565±3	72.00±0.25	0.2539±0.0038
^{40}Ca	763±2	70.07±0.25	0.2398±0.0042
^{52}Cr	343±4	70.05±0.25	0.2384±0.0052
^{58}Ni	338±5	70.03±0.25	0.2402±0.0042

As an example, Fig. 3 shows the scatter plot of the raw SSD signal versus the BV signal for the 800 MeV/nucleon ^{32}S beam. Dominating the plot is the strongly saturated sulfur beam spot, but there are also well-defined spots for fragments ranging from phosphorus to neon. Also seen in the plot are some background events, mostly due to interactions in the detectors and "pileup" effects, which must be identified and properly treated. After the background is corrected or removed [26], both the SSD and the BV signals are histogramed and Gaussian fits are performed to determine the charge peaks. Since the particles are close to minimum ionizing, the means of the Gaussian fits form a linear relationship with Z^2 and can be fitted with the least-squares method to provide the SSD charge calibration parameters. Due to saturation effects [28–30], the response of the BV plastic scintillator deviates significantly from a Z^2 dependence and was found to closely follow a linear relationship with Z, from beam charge (Z_B) down to $Z_B/2$ [26]. Therefore, the BV charge peaks are fit with a linear Z dependence to obtain the BV charge calibration. The final upstream post-target charge is a weighted combination of those from the SSD and the BV, with optimized weights of 3 to 1 in favor of the higher-resolution SSD detector, determined by minimizing the final charge uncertainties. Figure 4 shows the final unnormalized charge histogram (on a logarithmic scale) for both the target-in (solid curve) and the target-out (dashed curve) runs.

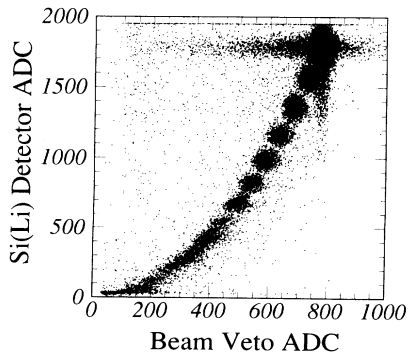

FIG. 3. SSD ADC vs BV ADC for ^{32}S at 800 MeV/nucleon with liquid-hydrogen target.

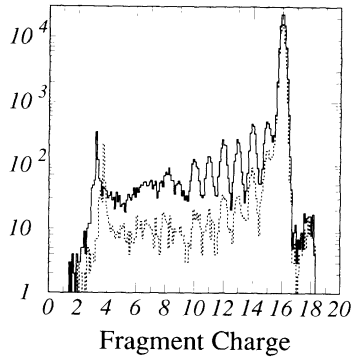

FIG. 4. Unnormalized charge histograms for ^{32}S at 800 MeV/nucleon with the liquid-hydrogen target (solid curve) and mass dummy target (dashed curve).

III. TOTAL CHARGE-CHANGING CROSS SECTIONS

A. Cross-section calculation

The total charge-changing cross section is defined here as the cross section for removing at least one charge from the beam projectile and neglects the small but finite cross sections for charge pickup [31]. Due to a finite time of flight (2–3 ns) between the target and SSD/BV, any fragments with a few nanoseconds or shorter lifetime would decay before being detected by post-target detectors. Instead, the decay products of such short-lived fragments were identified and, thus, considered as "direct" fragmentation products. The population of surviving particles that have the beam charge ($N_{\rm beam}$) can be written in the thin target case as (see Appendix for detail)

$$N_{\rm beam} = N_{\rm total} \cdot e^{-\sigma_{\Delta Z} \cdot t}, \tag{2}$$

and the population of particles that have undergone a charge-changing interaction ($N_{\rm frag} = N_{\rm total} - N_{\rm beam}$) is

$$N_{\rm frag} = N_{\rm total}(1 - e^{-\sigma_{\Delta Z} \cdot t}), \tag{3}$$

where $N_{\rm total}$ is the total number of valid incoming beam projectiles, $\sigma_{\Delta Z}$ is the total charge-changing cross section, and t is the effective "thickness" in mb^{-1} of the total amount of material traversed. In fact, the measured $N_{\rm frag}$ is affected by a background contribution that can be represented by a cross section (σ_B) and an effective thickness (t_B):

$$N_{\rm frag}^{\rm LH2} = N_{\rm total}^{\rm LH2}(1 - e^{-\sigma_{\Delta Z} \cdot t} \cdot e^{-\sigma_B \cdot t_B}), \tag{4}$$

where superscript LH2 denotes that data were taken with the liquid-hydrogen target. The background contribution is determined with runs using the mass dummy target. For these "target-out" (TO) runs the measured $N_{\rm frag}$ is

$$N_{\rm frag}^{\rm TO} = N_{\rm total}^{\rm TO}(1 - e^{-\sigma_B \cdot t_B}). \tag{5}$$

Combining Eqs. (4) and (5), the final cross section can be calculated:

$$\sigma_{\Delta Z} = \frac{1}{t} \ln \left(\frac{1 - N_{\rm frag}^{\rm TO}/N_{\rm total}^{\rm TO}}{1 - N_{\rm frag}^{\rm LH2}/N_{\rm total}^{\rm LH2}} \right) \ \text{(mb)} \tag{6}$$

and

$$t = \frac{N_A L}{A_H} \times 10^{-27} \ (\text{mb}^{-1}), \tag{7}$$

where $A_H = 1.00794$ is the atomic weight of hydrogen, $N_A = 6.022 \times 10^{23}$ is the Avogardro number, and L is the effective liquid-hydrogen target thickness in g/cm^2 (see Table II).

The surviving beam that has not undergone charge-changing interactions in the liquid-hydrogen target, $N_{\rm beam}$, is determined by fitting the beam charge peak in Fig. 4 with a Gaussian distribution. The total number of valid beams, $N_{\rm total}$, is determined by applying the beam definition cuts (see Sec. II) and summing the event scalers recorded for each proper trigger. From $N_{\rm total}$ and $N_{\rm beam}$, the fragment yield can be determined and Table III lists values of $N_{\rm total}^{\rm LH2}$, $N_{\rm frag}^{\rm LH2}$, $N_{\rm total}^{\rm TO}$, and $N_{\rm frag}^{\rm TO}$ for the different runs. These numbers can then be used with Eq. (6) to obtain the total charge-changing cross sections and the results are listed along with the associated uncertainties in Table IV.

The cross-section uncertainty is determined by the statistical and systematic errors in $N_{\rm frag}$ and is calculated using

$$\delta\sigma_{\Delta Z} = \sigma_{\Delta Z} \cdot \left[\left(\frac{\delta t}{t} \right)^2 + R^2 \right]^{1/2}, \tag{8}$$

where

$$R^2 = \left(\frac{\delta N_{\rm frag}^{\rm LH2}/(N_{\rm total}^{\rm LH2} - N_{\rm frag}^{\rm LH2})}{\Sigma} \right)^2 + \left(\frac{\delta N_{\rm frag}^{\rm TO}/(N_{\rm total}^{\rm TO} - N_{\rm frag}^{\rm TO})}{\Sigma} \right)^2 \tag{9}$$

and

$$\Sigma = \ln \left(\frac{1 - N_{\rm frag}^{\rm TO}/N_{\rm total}^{\rm TO}}{1 - N_{\rm frag}^{\rm LH2}/N_{\rm total}^{\rm LH2}} \right). \tag{10}$$

$N_{\rm total}$ is a defined quantity because of the beam definition cut, which removes any ambiguities such as beam contamination as well as detector and electronics irregularities. Consequently, it does not contribute to the final cross-section uncertainty. $N_{\rm frag}^{\rm LH2}$ and $N_{\rm frag}^{\rm TO}$ have both statistical and systematic uncertainties. The statistical uncertainty of the total charge-changing measurement, following the binominal distribution, is $\sqrt{N_{\rm total} \cdot p \cdot (1-p)}$, where p is the probability of a beam particle undergoing a charge-changing interaction. In our case, $p \ll 1$ and $\sqrt{N_{\rm total} \cdot p \cdot (1-p)} \approx \sqrt{N_{\rm frag}}$. Therefore, Poisson statistical uncertainties are applicable. The systematic uncertainty comes from the finite charge resolution between the Z_B and $Z_B - 1$ populations, as shown in Fig. 5, where hatched areas are the overlaps between two charge peaks (note the logarithmic scale). Because of the thin target used, the number of $Z_B - 1$ fragment itself is a small percentage of Z_B, and consequently the systematic uncertainty due to overlap is also small. Overall, the final uncertainties of the total charge-changing cross section measurements are about 3–6 %.

TABLE III. Measured beam and fragment numbers.

Beam	Energy (MeV/nucleon)	$N_{\rm total}^{\rm LH2}$	$N_{\rm frag}^{\rm LH2}$	$N_{\rm total}^{\rm TO}$	$N_{\rm frag}^{\rm TO}$
^{22}Ne	377±2	202 644	13 607±194	93 076	2 901±96
^{22}Ne	581±1	235 567	17 697±216	91 653	2 789±89
^{22}Ne	894±1	203 620	16 035±211	104 493	3 598±113
^{26}Mg	371±2	232 392	16 887±232	95 321	3 388±97
^{26}Mg	576±2	205 125	19 349±246	108 618	5 136±119
^{32}S	365±2	113 147	15 344±219	131 486	10 516±182
^{32}S	571±2	171 586	19 173±229	124 102	5 816±141
^{32}S	770±2	109 078	12 758±213	67 158	3 494±105
^{36}Ar	361±3	181 173	25 130±245	24 449	1 866±79
^{36}Ar	546±2	266 426	32 513±304	113 121	7 024±160
^{36}Ar	765±2	201 933	25 561±273	89 046	5 424±141
^{40}Ar	352±3	206 254	21 999±280	180 353	8 838±183
^{40}Ca	357±3	124 206	19 999±291	107 074	10 062±225
^{40}Ca	565±3	163 904	21 431±273	127 882	6 735±179
^{40}Ca	763±2	207 094	29 208±331	112 766	7 145±159
^{52}Cr	343±4	197 956	29 593±465	120 627	10 044±281
^{58}Ni	338±5	79 517	13 820±309	52 069	4 810±150

TABLE IV. Total charge-changing cross sections.

Beam	Energy (MeV/nucleon)	$\sigma_{\Delta Z}$ (mb)	$\delta\sigma_{\Delta Z}$ (mb)
^{22}Ne	377±2	264	10
^{22}Ne	581±1	327	9
^{22}Ne	894±1	329	11
^{26}Mg	371±2	288	13
^{26}Mg	576±2	359	13
^{32}S	365±2	409	16
^{32}S	571±2	470	14
^{32}S	770±2	494	18
^{36}Ar	361±3	474	27
^{36}Ar	546±2	463	15
^{36}Ar	765±2	531	21
^{40}Ar	352±3	446	16
^{40}Ca	357±3	508	22
^{40}Ca	565±3	567	16
^{40}Ca	763±2	604	18
^{52}Cr	343±4	526	27
^{58}Ni	338±5	655	38

B. Energy dependence

The total charge-changing cross sections from this work are plotted in Fig. 6 as a function of energy as solid symbols. Also shown are measurements from other experiments [10,32–34] (open symbols) and predictions from the semiempirical relations of Letaw *et al.* [1] (dotted line) and Garcia-Munoz *et al.* [2] (solid line). Both formulations predict total mass-changing cross sections and, to compare with the experimental data on charge-changing cross sections, the neutron-stripping cross sections calculated by Silberberg and Tsao [3] have been subtracted from the predictions. The Letaw *et al.* relation is an empirical fit to the total reaction cross sections for a proton beam on helium and heavier target nuclei, while the Garcia-Munoz *et al.* formula uses the energy dependence proposed by Karol [22], combined with a fit to a compilation of (p-p) and (p-n) total cross sections.

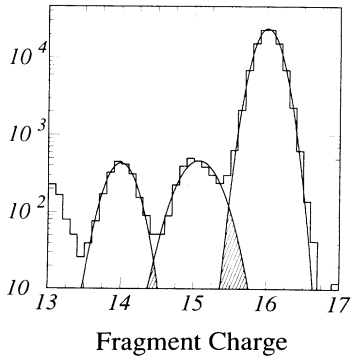

FIG. 5. Charge histogram for ^{32}S at 800 MeV/nucleon with the liquid-hydrogen target with only three leading charges Gaussian fits are shown as solid curves. Hatched areas are overlapped populations from adjacent charges.

The original Karol model is a modified semiclassical optical model that replaces the Bradt and Peters [21] hard-sphere nucleus with a soft sphere, using a realistic nuclear density distribution within the nucleus.

Comparison between our data and earlier measurements of the same projectiles over comparable energy ranges shows generally good agreement. Our 600 and 800 MeV/nucleon ^{32}S measurements are slightly above those from Webber *et al.* [10] at comparable energies, but still within experimental uncertainties. In the ^{36}Ar

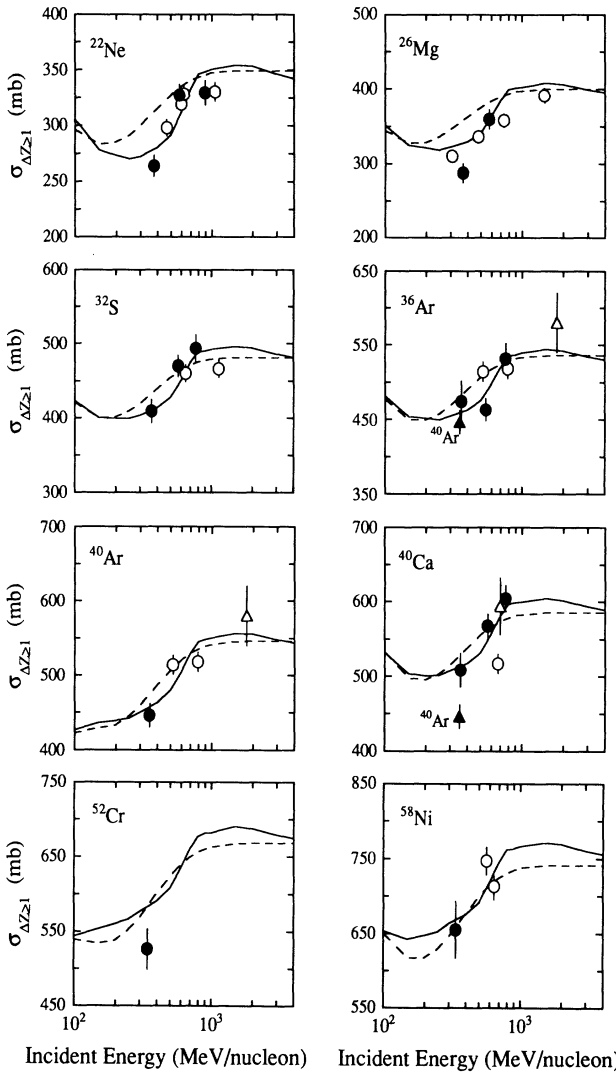

FIG. 6. Total charge-changing cross sections plotted as functions of incident beam energy. Data from this experiment are shown as solid circles. Open circles in ^{22}Ne are Webber *el al.* ^{20}Ne data [10]. Open circles in ^{26}Mg are Webber *et al.* ^{24}Mg data [10]. Open circles in ^{32}S are Webber *et al.* ^{32}S data [10]. Open circles in both ^{36}Ar and ^{40}Ar are Webber *et al.* ^{40}Ar data [10] and open triangle is Lindstrom *et al.* data [32]. Solid triangle in both ^{36}Ar and ^{40}Ca plots is ^{40}Ar from this experiment. Open circle in ^{40}Ca is Webber *et al.* ^{40}Ca data [10] and open triangle is Anderson *et al.* proton beam data [34]. Open circles in ^{58}Ni are Webber *et al.* data [10,33]. Dotted lines are Letaw *et al.* [1] predictions. Solid lines are Garcia-Munoz *et al.* [2] predictions.

plot we include other measurements from Webber *et al.* [10] (open circle), and Lindstrom *et al.* [32] (open triangle) and apart from one intermediate-energy point there is good agreement.

Compared with predictions, the overall conclusion is that both semiempirical formulas provide an adequate but not excellent fit to the measured cross sections. We notice in some instances that the Garcia-Munoz *et al.* relation predicts the trend in the data better, showing a stronger "dip" at intermediate energies. For example, the ^{22}Ne and ^{26}Mg plots show evidence for a strong energy dependence at low energies. In the ^{22}Ne plot, the open circles are Webber *et al.* measurements of ^{20}Ne [10], and the two sets trace each other very closely. Similar features also occur in the other neutron-rich species, ^{26}Mg, where the open circles are Webber *et al.* [10] measurements of ^{24}Mg. The heavier neutron-rich species, ^{52}Cr, is slightly below the predictions, while ^{58}Ni, which has only two excess neutrons, is in agreement with the predictions at our energy. The Webber *et al.* measurements for ^{58}Ni (open circles) [10,33] are also close to the predictions.

The neutron-rich isotopes seem to follow their neutron-balanced counterparts of the same charge, but fall below the beams that have the same number of total nucleons, indicating that mass number is probably not the only parameter of importance. This is illustrated in both the ^{36}Ar and the ^{40}Ca plots which include the cross section of ^{40}Ar from this experiment (solid triangle). One notices here that there is little difference between ^{36}Ar and ^{40}Ar. However, the total cross section of ^{40}Ar is considerably smaller than ^{40}Ca, even though ^{40}Ar and ^{40}Ca have the same mass. To confirm such an effect is indeed caused by nuclear composition, more studies are needed on similar systems.

Also included in the ^{40}Ca plot is a 700 MeV proton total reaction cross-section measurement (open triangle) on a ^{40}Ca target [34], with the neutron-stripping cross section subtracted. Even though this is a "reversed" process, compared to heavy-ion projectile fragmentation in hydrogen, the measured proton cross section fits well with our data, but is significantly different from the previous measurement [10] at 600 MeV/nucleon.

C. Mass dependence

The dependence of the total charge-changing cross sections on the projectile mass can be demonstrated through the Bradt-Peters [21] form of parametrization of a hard sphere with a finite overlap:

$$\sigma(A_B, A_T) = \pi r_0^2 (A_T^{1/3} + A_B^{1/3} - b)^2. \quad (11)$$

For proton-nucleus (p-A) collisions, the Bradt-Peters formula is not directly applicable since the so-called overlap parameter b as well as the scaled nucleus radius, $r_0 A_T^{1/3}$, cannot be directly applied to hydrogen. Different interpretations have been made so that Eq. (11) can be used. For example, Westfall *et al.* [17] arbitrarily chose $A_T = 0.089$ for hydrogen to fit their data. To address this problem, Hoang *et al.* [35] proposed a modified form for hadron-nucleus (h-A) interactions:

$$\sigma(A) = \pi r_0^2 \left[A^{1/3} - \left(\frac{\lambda}{2r_0} \right)^2 \cdot \frac{1}{A^{1/3}} \right]^2, \quad (12)$$

where λ is the absorption mean free path. This model was based upon high-energy p, $\bar{p}$, $\pi^{\pm}$, and $K^{\pm}$ data. At lower energy, the nuclear opacity, or "black nucleus" model, originally developed by Bethe [36], has been modified [37,38] to include a Coulomb repulsion term and a nuclear transparency term. However, in our particular beam and energy range these terms are quite negligible, making this approach equivalent to that of Hoang *et al.* Thus, the discussion on mass dependence of our data will be based upon the Hoang *et al.* model.

Figure 7 plots $\sigma_{\Delta Z}$ as a function of $(A_{\rm beam})^{2/3}$, for three energy groups: ~400 MeV/nucleon [Fig. 7(a)], ~600 MeV/nucleon [Fig. 7(b)], and 800–900 MeV/nucleon [Fig. 7(c)]. Here we also include measurements from other experiments with comparable energies [10,32–34,39–41]. The fit to Eq. (12) with fixed $r_0 = 1.35$ fm [17] is shown as the solid curve in Fig. 7. These values for λ are listed in Table V, along with the Hoang *et al.* value from high-energy proton beam data, and are plotted in Fig. 8(a). We also fit the data to Eq. (10) with $A_T = 0.089$ (dashed curves in Fig. 7), to compare with the Westfall *et al.* 1.88 GeV/nucleon ^{56}Fe data. The derived overlap parameter b is listed in Table VI and plotted in Fig. 8(b). Inspection of Fig. 7 suggests that Eq. (11) provides a slightly better representation of the data than does Eq. (12). However, neither is capable of getting a good fit to all the data, suggesting that a single-parameter representation is probably inadequate. Nevertheless, these models are very simple yet effective methods to organize the data over a large range of mass and energy. The dotted curves are the total mass-changing cross sections from Karol's model [22], scaled by a factor of 0.85. This model has a better trend prediction on ultraheavy species than the single-parameter models.

For the most part, the total cross sections follow the $A^{2/3}$ mass dependence. The fitted absorption mean free path λ of Eq. (12) [Fig. 8(a)] displays a clear energy dependence within the energy range covered by this experiment. Our λ values are over twice that obtained from proton data at 20 GeV [35], suggesting that the energy dependence continues to higher energy. The overlap parameter b from Eq. (11) [Fig. 8(b)] also shows an energy dependence in our energy range, and our highest-energy value is consistent with the result obtained at 1.8 GeV/nucleon [17]. One note of caution is that the fitting results are, in essence, average values across all the pro-

TABLE V. Fitted parameter λ for Hoang *et al.* model.

Energy (MeV/nucleon)	λ (fm)
403±65	3.12±0.03
597±81	2.82±0.03
945±221	2.71±0.03
20 000[a]	1.29±0.01[a]

[a]Hoang *et al.* value [35].

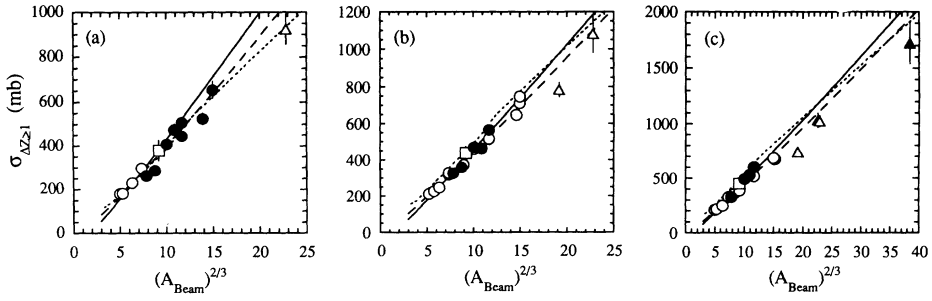

FIG. 7. Mass dependence of total charge-changing cross sections: (a) ~400 MeV/nucleon; (b) ~600 MeV/nucleon; (c) 800–900 MeV/nucleon. Solid lines are the fitted Hoang *et al.* model [Eq. (12)]. Dashed lines are the fitting of Eq. (11). Dotted lines are the calculated total mass-changing cross sections from Karol's model [22], scaled by a factor of 0.85. Solid circles are from this experiment. Open circles are various Webber *et al.* data [10,33]. Open square is Crawford *et al.* ^{28}Si data [39]. Open triangles are Nilsen *et al.* ^{84}Kr and ^{109}Ag data [40]. Solid triangles is Greiner *et al.* ^{238}U data [41]. Some of the data points with identical mass have been shifted slightly to clarify the plot.

jectiles, with no consideration of the nuclear structure. The result of this model comparison is the verification of the energy dependence in the total charge-changing cross sections discussed in connection with Fig. 6.

The results in Figs. 6 and 7 show a tendency for the neutron-rich species to have smaller cross sections with respect to the predictions. This implies that charge-changing total cross sections depend not only on total mass, but also on the neutron-to-proton ratio or isospin of the projectile nuclei. This effect is investigated in Fig. 9 where the cross section per nucleon, $\sigma_{\Delta Z\geq 1}/A$, is plotted as a function of the neutron-to-proton (n/p) ratio for the same three energy bins as in Fig. 7. Here we include data from still heavier projectiles [10,32–34] to extend the n/p ratio. There is a general trend for the per nucleon total charge-changing cross section to decrease as the n/p ratio increases from 1, most notable in the 400 MeV/nucleon data [Fig. 9(a)]. In all cases there is a transition at $n/p \sim 1.3$ corresponding to nuclei with $A > 80$. Part of this trend is caused by the mere existence of excess neutrons, which do not contribute to the total charge-changing interactions. However, scaling the data by a factor of $A/2Z$ (which removes the excess neutrons share of the per nucleon $\sigma_{\Delta Z\geq 1}$) does not significantly change the overall trend. The interesting observation here is that adding more neutrons seems to decrease the total charge-changing interaction cross sections. It is likely that neutron-rich nuclei may have larger neutron-stripping cross sections, since the excess neutrons can be removed more easily during the collision. Experimental investigations [42–44] of ^{11}Li, a very neutron-rich species, indicate that there is a tail in the distribution of nuclear matter, forming a halolike structure around the nucleus. Also, a strong isospin dependence of lighter (Be-B) nuclear radii has been observed [45], indicating again that the neutron-to-proton ratio plays an important role in the nuclear structure and the interaction cross sections. However, it is not clear why, from a simple shell-model approach, the charge-changing total cross sections should be reduced. It is possible that there are residual contributions to this effect from the combination of the general

TABLE VI. Fitted parameter b for optical model.

Energy (MeV/nucleon)	b (fm)
403±65	0.97±0.01
597±81	0.84±0.01
945±221	0.82±0.01
1880[a]	0.83±0.12[a]

[a]Westfall *et al.* ^{56}Fe at 1.88 GeV/nucleon [17].

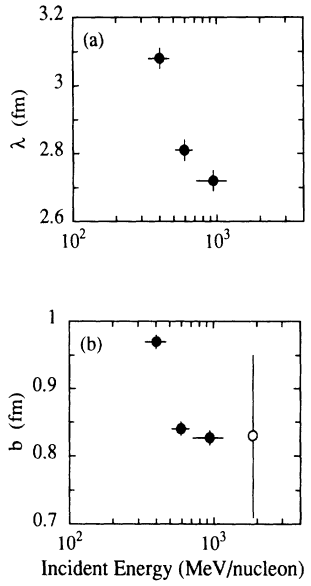

FIG. 8. (a) Fitted absorption mean free path λ vs incident beam energy. (b) Fitted values of the overlap parameter b vs incident beam energy. The bars along the energy axis are the total energy span of all the data used in the fit. Open circle is Westfall *et al.* ^{56}Fe at 1.88 GeV/nucleon data [17].

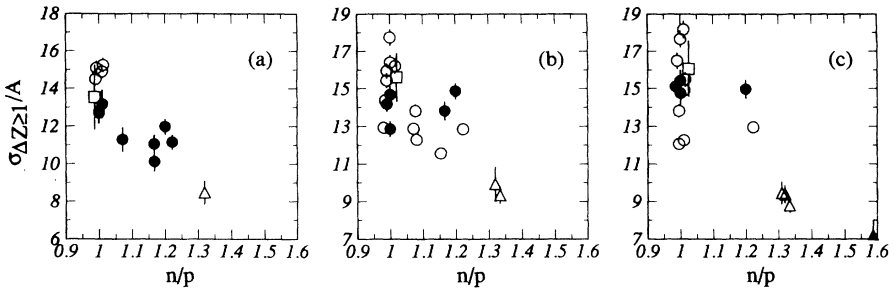

FIG. 9. Per nucleon total charge-changing cross sections plotted against neutron-to-proton ratio (n/p): (a) ~400 MeV/nucleon; (b) ~600 MeV/nucleon; (c) 800–900 MeV/nucleon. Beams with exactly the same n/p ratio have been shifted slightly to clarify the plots. See Fig. 7 for symbols and references.

$A^{2/3}$ dependence of cross sections combined with a weak $A^{1/3}$ dependence of n/p ratio for stable nuclei. Further investigation of neutron-stripping cross sections and momentum distributions of beam charge isotopes are needed to shed light on this problem and our studies of the elemental and isotopic cross sections will address this issue.

As a comparison, we also plot the derived mass-changing cross sections in Fig. 10, where the neutron-stripping portion of the cross sections is either estimated from the Silberberg and Tsao semiempirical formula [3], with an assigned 20% uncertainty, or is taken, if available, from experimental data [12]. The overall mass dependence remains the same, with some improvement in the clustering for the 400 MeV/nucleon results (cf. Fig. 7). Also plotted are fits for the Hoang *et al.* [35] model (solid line), the Westfall *et al.* form [17] with $A_T = 0.089$ (dashed line), and the Sihver *et al.* [5] empirical predictions (dot-dashed line), which assumes an energy-independent fitting of total cross sections beyond 200 MeV/nucleon. The latter two predictions are almost identical at 400 MeV/nucleon, and separate slightly at higher energies. The dotted curve is Karol's soft-sphere model prediction of total mass-changing cross sections. In general, the agreement with the data is good. However, one must be careful in drawing firm conclusions from Fig. 10 since it is difficult to assess the accuracy of the calculated neutron-stripping cross sections.

IV. CONCLUSIONS

We have measured total charge-changing cross sections for 17 different beam-energy combinations in the energy range 400–900 MeV/nucleon, using a liquid-hydrogen target to make direct measurements of heavy-ion cross sections in hydrogen instead of relying on the CH_2-C subtraction technique. The measured total charge-changing cross sections show an energy dependence which follows closely the predictions of the semiempirical models. Interpreted in terms of an optical model for nucleon-nucleus collisions, the results demonstrated that, within the experimental energy range, the optical-model parameters have a clear energy dependence. The measured cross sections are well scaled by $A^{2/3}$, but appear to depend, as well, on the isospin of the fragmenting nucleus. Thus, in the energy range of the nuclear species investigated, the total cross-section results point out that both energy and nucleus composition play significant roles in heavy-ion fragmentation. Further investigation of elemental charge-changing processes and isotopic production cross

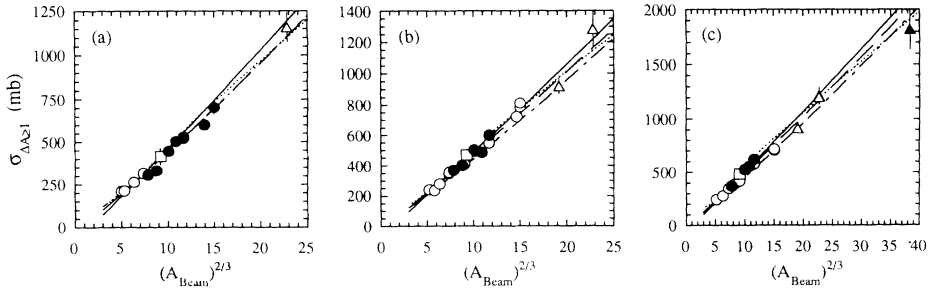

FIG. 10. Mass dependence of total mass-changing cross sections: (a) ~400 MeV/nucleon; (b) ~600 MeV/nucleon; (c) 800–900 MeV/nucleon. Solid lines are the fitted Hoang *et al.* model [35]. Dashed lines are the fit to Eq. (10). Dot-dashed lines are Sihver *et al.* [5] predictions. Dotted lines are Karol's model [22] predictions. Some of the data points with identical mass have been shifted slightly to clarify the plot. See Fig. 7 for symbols and references.

sections are needed to elucidate the details of these reactions.

ACKNOWLEDGMENTS

The Collaboration thanks the LBL Bevalac staff for their support during the experiment. Thanks are also due to I. Flores, S. Ko, C. Kuo, and J. Mazotta. This work was supported at Louisiana State University by NASA under Grant NAGW-1526 and by DOE under Grant DE-FG05-ER 40147; at University of California, Berkeley by NASA under Grant NGR 05-003-513; at University of Minnesota by NASA under Grant NAGW-2004; at Lawrence Berkeley Laboratory in part by NASA under Grant L14230C; at New Mexico State University by NASA under Grant NAGW-3022; and at Universita' di Catania by INFN, Italy.

APPENDIX

Equation (2) is an approximation to calculate the total charge-changing cross section $\sigma_{\Delta Z}$, under the thin target approximation. Since $\sigma_{\Delta Z}$ is a part of the total cross section σ_T,

$$\sigma_T = \sigma_{\Delta Z} + \sigma_n, \tag{A1}$$

where σ_n is the neutron-stripping cross section, then the true uninteracted (surviving) beam

$$N^0_{\text{beam}} = N_{\text{total}} \cdot e^{-\sigma_T t}, \tag{A2}$$

and total fragment population is

$$\begin{aligned} N^0_{\text{frag}} &= N_{\text{frag}} + N_n \\ &= N_{\text{total}} - N^0_{\text{beam}} \\ &= N_{\text{total}} \cdot (1 - e^{-\sigma_T t}), \end{aligned} \tag{A3}$$

where N_n is the $\Delta Z = 0$ fragment population and N_{frag} is $\Delta Z > 0$ (charge-changing) fragment population. Consequently, we have

$$N_{\text{frag}} = N_{\text{total}} \cdot (1 - e^{-\sigma_T t}) \cdot \frac{\sigma_{\Delta Z}}{\sigma_T}. \tag{A4}$$

However, our experiment was not designed to directly measure σ_T. By substituting Eq. (A1) into Eq. (A3), we have

$$N^0_{\text{frag}} = N_{\text{total}} \cdot (1 - e^{-\sigma_{\Delta Z} t} \cdot e^{-\sigma_n t}). \tag{A5}$$

In order to obtain the total charge-changing cross sections, we apply the thin target approximation. For a thin target, $\sigma t \ll 1$, Eq. (A5) can be expanded into linear form:

$$\begin{aligned} N^0_{\text{frag}} &= N_{\text{total}} \cdot [1 - (1 - \sigma_{\Delta Z} t) \cdot (1 - \sigma_n t)] \\ &= N_{\text{total}} \cdot (\sigma_{\Delta Z} t + \sigma_n t). \end{aligned} \tag{A6}$$

By comparing Eq. (A6) and Eq. (A3), we have

$$N_{\text{frag}} = N_{\text{total}} \cdot \sigma_{\Delta Z} t, \tag{A7}$$

which is equivalent to a cross-section-like equation:

$$N_{\text{frag}} = N_{\text{total}} \cdot (1 - e^{-\sigma_{\Delta Z} t}). \tag{A8}$$

Thus, we can calculate the total charge-changing cross section without knowing the total reaction cross section, since Eq. (A8) requires only the incoming beam and $\Delta Z > 0$ fragments. The difference between Eqs. (A8) and (A4) is smaller than a second-order term of the Taylor expansion.

[1] J. R. Letaw, R. Silberberg, and C. H. Tsao, Astrophys. J. Suppl. Ser. **51**, 271 (1983).
[2] M. Garcia-Munoz, J. A. Simpson, T. G. Guzik, J. P. Wefel, and S. H. Margolis, Astrophys. J. Suppl. Ser. **64**, 269 (1987).
[3] R. Silberberg and C. H. Tsao, in *Proceedings of the 20th International Cosmic Ray Conference*, Moscow, 1987, edited by V. A. Kozyarivsky, A. S. Linvansky, T. I. Tulupova, A. L. Tsyabuk, A. V. Voevodsky, and N. S. Volgemut (NAUKA, Moscow, 1987), Vol. 2, p. 133.
[4] C. H. Tsao, R. Silberberg, A. F. Barghouty, L. Sihver, and T. Kanai, Phys. Rev. C **47**, 1257 (1993).
[5] L. Sihver, C. H. Tsao, R. Silberberg, T. Kanai, and A. F. Barghouty, Phys. Rev. C **47**, 1225 (1993).
[6] W. R. Webber, J. C. Kish, and D. A. Schrier, Phys. Rev. C **41**, 566 (1990).
[7] G. M. Raisbeck and F. Yiou, in *Spallation Nuclear Reactions and Their Applications*, edited by B. S. P. Shen and M. Merker (Dordrecht, Reidel, 1975), p. 83.
[8] T. G. Guzik, in *Particle Astrophysics*, AIP Conf. Proc. No. 203, edited by W. V. Jones, F. J. Kerr, and J. F. Ormes (AIP, New York, 1990), p. 275.
[9] W. R. Binns, T. L. Garrard, M. H. Isreal, M. P. Kertzmann, J. Klarmann, E. C. Stone, and C. J. Waddington, Phys. Rev. C **36**, 1870 (1987).
[10] W. R. Webber, J. C. Kish, and D. A. Schrier, Phys. Rev. C **41**, 520 (1990).
[11] W. R. Webber, J. C. Kish, and D. A. Schrier, Phys. Rev. C **41**, 533 (1990).
[12] W. R. Webber, J. C. Kish, and D. A. Schrier, Phys. Rev. C **41**, 547 (1990).
[13] B. G. Harvey, Phys. Rev. Lett. **47**, 454 (1981).
[14] W. U. Schroeder and J. R. Huizenga, Annu. Rev. Nucl. Sci. **27**, 465 (1977).
[15] H. H. Heckman, D. E. Greiner, P. J. Lindstrom, and F. S. Bieser, Phys. Rev. Lett. **28**, 926 (1972).
[16] P. Kirkby and W. T. Link, Can. J. Phys. **44**, 1847 (1966).
[17] G. D. Westfall, L. W. Wilson, P. J. Lindstrom, H. J.

Crawford, D. E. Greiner, and H. H. Heckman, Phys. Rev. C **19**, 1309 (1979).
[18] C. Perrin, S. Kox, N. Longequeue, J. B. Viano, M. Buenerd, R. Cherkaoui, A. J. Cole, A. Gamp, J. Menet, R. Ost, R. Bertholet, C. Guet, and J. Pinston, Phys. Rev. Lett. **49**, 1905 (1982).
[19] A. J. Cole, W. D. M. Rae, M. E. Brandan, A. Decal, B. G. Harvey, R. Legrain, M. J. Murphy, and R. G. Stokstad, Phys. Rev. Lett. **47**, 1705 (1981).
[20] J. Jaros, A. Wagner, L. Anderson, O. Chamberlain, R. Z. Fuzesy, J. Gallup, W. Gorn, L. Shroeder, D. Shannon, G. Shapiro, and H. Steiner, Phys. Rev. C **18**, 2273 (1978).
[21] H. C. Bradt and B. Peters, Phys. Rev. **77**, 54 (1950).
[22] P. J. Karol, Phys. Rev. C **11**, 1203 (1975).
[23] T. G. Guzik, S. Albergo, Z. Caccia, C.-X. Chen, S. Costa, H. J. Crawford, J. Engelage, P. Ferrando, I. Flores, L. Greiner, F. C. Jones, C. N. Knott, S. Ko, P. J. Lindstrom, J. Mazotta, J. W. Mitchell, R. Potenza, J. Romanski, G. V. Russo, A. Soutoul, O. Testard, C. E. Tull, C. Tuvé, C. J. Waddington, W. R. Webber, J. P. Wefel, and X. Zhang, Adv. Space Res. (in press).
[24] J. Engelage, M. E. Baumgartner, E. Beleal, B. L. Berman, F. Bieser, F. P. Brady, M. Bronson, H. J. Crawford, I. Flores, D. E. Greiner, L. Greiner, O. Hashimoto, G. Igo, S. Kadota, P. N. Kirk, P. J. Lindstrom, C. McParland, S. Nagamiya, D. L. Olson, J. Porter, J. L. Romero, C. L. Ruiz, T. J. M. Symons, I. Tanihata, R. Wada, M. L. Webb, J. Yamada, and H. Yee, Nucl. Instrum. Methods Phys. Rev. A **277**, 431 (1989).
[25] J. Engelage, S. Albergo, C.-X. Chen, S. Costa, H. J. Crawford, P. Ferrando, L. Greiner, T. G. Guzik, F. C. Jones, C. N. Knott, S. Ko, C. Kuo, P. J. Lindstrom, U. Lynen, J. Mazotta, J. W. Mitchell, W. F. J. Mueller, D. Olson, R. Potenza, A. Soutoul, T. J. M. Symons, O. Testard, C. E. Tull, C. Tuvé, C. J. Waddington, W. R. Webber, J. P. Wefel, and H. H. Wieman, in *Proceedings of the 22nd International Cosmic Ray Conference*, Dublin, 1991, edited by M. Cawley, L. O'C. Drury, D. J. Fegan, D. O'Sullivan, N. A. Porter, J. J. Quenby, and A. A. Watsen (Dublin Institute for Advanced Studies, Dublin, 1991), Vol. 2, p. 531.
[26] J. Engelage, S. Albergo, Z. Caccia, C.-X. Chen, S. Costa, H. J. Crawford, M. Cronqvist, P. Ferrando, R. Fonte, L. Greiner, T. G. Guzik, A. Insolia, F. C. Jones, C. N. Knott, S. Ko, C. Kuo, P. J. Lindstrom, J. Mazotta, J. W. Mitchell, R. Potenza, J. Romanski, G. V. Russo, A. Soutoul, O. Testard, C. E. Tull, C. Tuvé, C. J. Waddington, W. R. Webber, J. P. Wefel, and X. Zhang, to be submitted to Nucl. Instrum. Methods Phys. Res. A.
[27] S. Albergo, S. Costa, M. Mazzeo, D. Nicotra, G. Poli, R. Potenza, C. Tuvé, H. J. Crawford, and I. Flores, Nucl. Instrum. Methods Phys. Res. A **311**, 280 (1992).
[28] R. Dwyer and D. Zhou, Nucl. Instrum. Methods Phys. Res. A **242**, 171 (1985).
[29] M. H. Salamon and S. P. Ahlen, Nucl. Instrum. Methods **195**, 557 (1982).
[30] S. P. Ahlen, B. G. Cartwright, and G. Tarlé, Nucl. Instrum. Methods **147**, 321 (1977).
[31] W. R. Binns, J. R. Cummings, T. L. Garrard, M. H. Isreal, J. Klarmann, E. C. Stone, and C. J. Waddington, Phys. Rev. C **39**, 1785 (1989).
[32] P. J. Lindstrom, D. E. Greiner, H. H. Heckman, B. Cork, and F. S. Bieser, in *Proceedings of the 14th International Cosmic Ray Conference*, Munich, 1975 (Max-Planck Institute, Munich, 1975), Vol. 7, p. 2315.
[33] W. R. Webber *et al.* (private communication).
[34] B. D. Anderson, P. R. Bevington, F. H. Cverna, M. W. McNaughton, H. B. Willard, R. J. Barrett, N. S. P. King, and D. J. Ernst, Phys. Rev. C **19**, 905 (1979).
[35] T. F. Hoang, B. Cork, and H. J. Crawford, Z. Phys. C **29**, 611 (1985).
[36] H. A. Bethe, Phys. Rev. **57**, 1125 (1940).
[37] S. Fernbach, R. Serber, and T. B. Taylor, Phys. Rev. **75**, 1352 (1949).
[38] M. M. Shapiro, Phys. Rev. **90**, B17 (1953).
[39] H. J. Crawford, J. Engelage, T. G. Guzik, J. Isbert, P. J. Lindstrom, J. W. Mitchell, J. J. Pitts, W. Schimmerling, M. Simon, and J. P. Wefel, in *Proceedings of the 21st International Cosmic Ray Conference*, Adelaide, 1990, edited by R. J. Protheroe (University of Adelaide, Adelaide, 1990), Vol. 3, p. 408.
[40] B. S. Nilsen, C. J. Waddington, J. R. Cummins, W. R. Binns, T. L. Garrard, and J. Klarmann, in *Proceedings of the 23rd International Cosmic Ray Conference*, Calgary, 1993 (University of Calgary, Calgary, 1993), Vol. 2, p. 195.
[41] D. E. Greiner, H. Crawford, P. J. Lindstrom, J. M. Kidd, D. L. Olson, W. Schimmerling, and T. J. M. Symons, Phys. Rev. C **31**, 416 (1985).
[42] I. Tanihata, H. Hamagaki, O. Hashimoto, Y. Shida, N. Yoshikawa, K. Sugimoto, O. Yamakawa, T. Kobayashi, and N. Takahashi, Phys. Rev. Lett. **55**, 2676 (1985).
[43] T. Kobayashi, O. Yamakawa, K. Omata, K. Sugimoto, T. Shimoda, N. Takahashi, and I. Tanihata, Phys. Rev. Lett. **60**, 2599 (1988).
[44] T. Kobayashi, S. Shimoura, I. Tanihata, K. Katori, K. Matsuta, T. Minamisono, K. Sugimoto, W. Müller, D. L. Olson, T. J. M. Symons, and H. Wieman, Phys. Lett. B **232**, 51 (1989).
[45] I. Tanihata, T. Kobayashi, O. Yamakawa, S. Shimoura, K. Ekuni, K. Sugimoto, N. Takahashi, T. Shimoda, and H. Soto, Phys. Lett. B **206**, 592 (1988).